

Article

Impact of a New Radiation Scheme on Simulated Climate in the Global–Regional Integrated System Model under Varying Physical Parameterization Schemes

Chang Yuan ¹, Hua Zhang ², Xianwen Jing ^{2,3,*} , Shuyun Zhao ¹ and Xiaohan Li ⁴

¹ Department of Atmospheric Science, School of Environmental Studies, China University of Geosciences, Wuhan 430074, China; changyuan@cug.edu.cn (C.Y.); zhaosy@cug.edu.cn (S.Z.)

² State Key Laboratory of Severe Weather, Chinese Academy of Meteorological Sciences, Beijing 100081, China; huazhang@cma.gov.cn

³ College of Urban and Environmental Sciences, Hubei Normal University, Huangshi 435002, China

⁴ Department of Earth System Science, Tsinghua University, Beijing 100084, China; lixh@cma.gov.cn

* Correspondence: jingxw@hbnu.edu.cn

Abstract: In this study, the radiation scheme BCC-RAD (Beijing Climate Center RADIative transfer model) developed for global climate models is implemented into the Global–Regional Integrated System (GRIST) model as an alternative to the default RRTMG (general circulation model (GCM) version of the Rapid Radiative Transfer Model) scheme. Its impact on the simulated climate is comprehensively evaluated under different physics parametrization packages, in comparison with both the CERES (partly from ERA5 reanalysis) observations and multi-model results from CMIP6. The results indicate that under the default physics parameterization package of GRIST (PhysC), BCC-RAD improved the simulated global mean cloud cover by ~3% and the clear-sky outgoing longwave radiation by ~5.6 W/m². Upon the inclusion of the PhysCN parameterization package, BCC-RAD exhibited further improvement in simulated cloud cover and radiative forcing (particularly longwave radiative forcing, the bias of which decreases from –9.2 W/m² to –1.8 W/m²), leading it to be closer to observations than RRTMG. Additionally, BCC-RAD improved the simulation of atmospheric temperature and hence notably diminished the apparent overestimation of atmospheric humidity seen in RRTMG. This study demonstrates the advantages of BCC-RAD over RRTMG in certain aspects of the GRIST-simulated climate, verifying its capability for the climate-oriented configuration of GRIST.

Keywords: BCC-RAD; GRIST; climate simulation; radiation scheme evaluation



Citation: Yuan, C.; Zhang, H.; Jing, X.; Zhao, S.; Li, X. Impact of a New Radiation Scheme on Simulated Climate in the Global–Regional Integrated System Model under Varying Physical Parameterization Schemes. *Atmosphere* **2024**, *15*, 501. <https://doi.org/10.3390/atmos15040501>

Academic Editor: Hui Zhao

Received: 17 March 2024

Revised: 7 April 2024

Accepted: 17 April 2024

Published: 19 April 2024



Copyright: © 2024 by the authors. Licensee MDPI, Basel, Switzerland. This article is an open access article distributed under the terms and conditions of the Creative Commons Attribution (CC BY) license (<https://creativecommons.org/licenses/by/4.0/>).

1. Introduction

An accurate depiction of the radiative transfer processes is fundamental to the realistic simulation of both the global climate system and local weather evolutions. Many factors inhibit the precise representation of radiation transfer processes in models, such as biases in cloud and aerosol optical properties, assumptions about unresolved cloud morphology, inaccuracies introduced by simplified radiation transfer algorithms, and approximations in gas absorption treatments [1–3]. The above uncertainties in radiative transfer calculations are more pronounced in models that integrate the capability of weather forecast and climate simulation in a single framework, which has become a current trend of Earth system modeling. This is because the grid resolution in such models can range from a few kilometers to tens or hundreds of kilometers, whether in a single run (with varying grid sizes) or in separate runs with different purposes, posing extra challenges to the reliability of the treatment of unresolved phenomenon (e.g., inhomogeneous distribution of cloud particles, vertical overlap of cloud cover) in the radiative transfer scheme.

With the development of Earth System Models, as well as the continuously increasing computing power, weather- and climate-integrated models have gained momentum in

recent years. For example, the LFRic model system [4] developed by the Met Office of the UK, the ICON model [5,6] developed by the German Weather Service and the Max Planck Institute for Meteorology, and the NICAM model [7] jointly developed by the Atmosphere and Ocean Research Institute and the Japan Agency for Marine-Earth Sciences and Technology. Against this backdrop, the State Key Laboratory of Severe Weather at the Chinese Academy of Meteorological Sciences has also started to develop its own weather/climate-integrated model, i.e., the Global-to-Regional Integrated Forecast SysTEM (GRIST). GRIST utilizes variable-resolution (VR) grid technology as its dynamic framework, which, by increasing grid density in key areas while decreasing grid density in remote areas in its global simulations, is potentially capable of better representation of small-scale physical processes in the targeted areas; meanwhile, it is free from any boundary condition problems, as is the case for traditional regional models. It aims to meet various application demands, such as high-resolution weather/climate prediction spanning from tens to thousands of kilometers and long-term climate simulations [8].

The VR model framework requires the treatment of physical processes, e.g., the radiative transfer process, to not only be physically more robust but also more adaptable to its varying resolution. The BCC-RAD radiation scheme (i.e., the Beijing Climate Center Radiative transfer model), developed by Zhang et al. [9,10] (hereafter referred to as the new scheme) and previously implemented in the global climate model BCC_AGCM2.0.1 [10], was demonstrated to lead to improvements in clear-sky radiation flux, cloud radiation forcing, atmospheric temperature, and other related factors in the BCC_AGCM2.0.1 model [10] compared with RRTMG (the original radiation scheme of both BCC_AGCM2.0.1 and GRIST, hereafter referred to as the old scheme). Key advances of BCC-RAD in recent years include fundamental improvements in its particle optics and radiative transfer algorithm: (1) a sophisticated parameterization of ice cloud optics considering contributions from various ice crystal shapes based on observed ice shape composition; (2) newly calculated non-spherical aerosol optical parameters [11] and a method for calculating optical properties for mixed aerosols [12,13]; (3) a four-stream discrete ordinate cumulative radiative transfer algorithm that is more accurate than the conventional two-stream algorithm to depict radiative transfer in clouds and aerosols [14]. Moreover, BCC-RAD has also incorporated the Monte Carlo Independent Column Approximation (McICA [10]) method to address the sub-grid variations in cloud condensate in a more flexible and more adjustable manner, rendering the cloud horizontal and vertical structures used in the radiation module capable to be tuned according to grid sizes [10]. Hence, the BCC-RAD radiation scheme is anticipated to be more compatible with the VR framework of the GRIST model.

Aiming at improving the representation of radiation processes by GRIST, this study integrates BCC-RAD into the GRIST model and documents the impact on simulated climate by comparing simulations with the original radiation scheme RRTMG and corresponding observations. It should be noted that, as a pilot evaluation of BCC-RAD in GRIST, this study concentrates on the basic global-constant resolution version of GRIST; the performance of BCC-RAD in a VR version of GRIST is left for our following study. Considering that radiation budgets also rely on moist physical processes involving clouds and precipitation, we also explore the impact of different coupling schemes between radiation and moist physics packages on climate simulations. The comparison between different radiation schemes under varying parameterization schemes can reveal whether the biases in simulated radiation budget stem from the radiation schemes or from the moist parameterizations, which is important for the identification of sources of model uncertainties. Two moist physics parameterization packages are available in GRIST. One is based on a mature set of CAM5.3 physics packages [15]. The other is developed by Li et al. [15] including a unified deep-shallow convection double-plume (DP) parameterization scheme [16], GaussPDF cloud macrophysics [17], and single-ice (SI) cloud microphysics [18].

The structure of this paper is as follows: Section 2 provides a detailed introduction to the GRIST model, as well as the RRTMG and BCC-RAD radiation scheme. Section 3

introduces the observational data used and the design of the experiments. Section 4 presents the experimental results, and Section 5 provides a brief discussion and the main conclusions.

2. Model Description

2.1. The GRIST Model

The Global-to-Regional Integrated Forecast SysTem (GRIST) is a unified model system for global weather and climate modeling [19–22]. GRIST supports spherical centroid Voronoi tessellation (SCVT [23,24]). Detailed information about GRIST can be found in the GRIST model tutorial on GitHub (<https://grist-tutorial.readthedocs.io/en/latest/features.html> (accessed on 2 February 2024)). The release version used in this study is GRIST-A23.6.26.

GRIST features a unified dynamics–physics coupling interface, which can couple different types of physical parameterization suites for various application scenarios. The original physics parameterization package in GRIST (referred to as PhysC [25]) is imported from the global Community Atmosphere Model (CAM5.3) [15]. PhysC contains ZM (Zhang–McFarlane) [26,27] deep convection, UW (University of Washington) [28] shallow convection, Park macrophysics [17], and MG08 microphysics (Morrison–Gettelman [29]). On the basis of PhysC, Li et al. [15] made some adjustments and formed a new physics parameterization package (PhysCN, hereinafter). PhysCN replaces the moist physics with the DP convection scheme [16], GaussPDF macrophysics [17], and single-ice microphysics [18]. Compared to PhysC, PhysCN reduces the precipitation over tropical oceans, enhances ice cloud formation near the tropospheric top in tropical regions, and improves the longwave cloud radiative forcing (LWCF) simulated by GRIST [15].

The original radiation scheme used in GRIST-A23.6.26 is RRTMG, i.e., the version of the Rapid Radiative Transfer Model (RRTM [30]) applied to the general circulation models (GCMs), which computes longwave and shortwave radiation flux using the correlated-k method (CKD). This scheme has found widespread application in GCMs, for instance, the ECMWF weather forecast system, the NCEP GFS model, the Community Earth System Model (CESM), the WRF model, and others [31–33].

2.2. BCC-RAD Radiation Scheme

In this study, the BCC-RAD radiation scheme [9,14,34,35] is incorporated into GRIST. BCC-RAD divides the whole radiation spectrum into 17 bands, including 8 longwave bands and 9 shortwave bands. BCC-RAD employs a four-stream radiative transfer algorithm to calculate radiation and a semi-random method to calculate cloud vertical overlap [36], respectively. The effective absorption coefficients of greenhouse gases mainly considered by BCC-RAD are calculated using the correlated-K-distribution method [34]. The calculation for the aerosol optical properties follows Wei and Zhang [37] and Zhang et al. [38]. The optical properties of cloud droplets are initially derived from Nakajima et al. [39] and subsequently improved based on the correlated-K method by Lu et al. [40]. The optical properties of ice crystals are calculated with consideration of various shapes of crystals combined based on optical datasets from Fu [41] and Yang et al. [42] and observed crystal shape composition from Baum et al. [43].

The BCC-RAD differs from the RRTMG scheme mainly in terms of the type of absorbing gases, the division between longwave and shortwave radiation ranges, liquid and ice cloud optics, and the representation of sub-grid cloud overlap (see Table 1). Note that both BCC-RAD and RRTMG use the Monte-Carlo independent column approximation method (McICA [10]) to treat cloud overlap; however, RRTMG applies the conventional Maximum-Random overlap (MRO) assumption to generate the sub-grid distribution of clouds, which is known to have systematic biases and is easily affected by the horizontal and vertical resolution of models [11]. In contrast, BCC-RAD applies a more realistic e-folding algorithm, which is less resolution-sensitive than MRO, to generate sub-grid cloud distribution. Improvements have been made to the e-folding algorithm based on satellite observations [44] and global cloud-resolving simulations [45], so that the cloud overlap

treatment is not static but is cloud system-aware. Hence, the advances in the BCC-RAD model make it potentially more suitable for the VR structure of GRIST.

Table 1. Comparison of the old (RRTMG) and new (BCC-RAD) radiation schemes.

	Old (RRTMG)	New (BCC-RAD)
Absorbing gases in LW	H ₂ O, CO ₂ , and O ₃ CH ₄ , N ₂ O, CFC ₁₁ , CFC ₁₂ , CFC ₂₂ , CCL ₄ [33]	H ₂ O, CO ₂ , and O ₃ CH ₄ , N ₂ O, CFC ₁₁ , CFC ₁₂ , CFC ₂₂
Absorbing gases in SW	H ₂ O, CO ₂ , O ₃ , and O ₂	H ₂ O, CO ₂ , O ₃ , N ₂ O, and O ₂
Range of LW	10–3250 cm ⁻¹ [30]	10–2680 cm ⁻¹
Range of SW	2600–50,000 cm ⁻¹	2110–49,000 cm ⁻¹
Band transmittance scheme	CKD scheme LW: emissivity formulations [46]; SW: formulas of Slingo [47] for liquid and of Ebert and Curry [46] for ice	CKD scheme Ice cloud: computed using data from Fu [41], Yang et al. [42], and Hong et al. [48]
Cloud optics		
Cloud overlap	McICA with Maximum-Random overlap	McICA with observation-based e-folding overlap

3. Experimental Design

In this study, we comprehensively investigate the performance of BCC-RAD in comparison with RRTMG. Single Column Model (SCM) and full general circulation model (GCM) simulations are performed. The SCM basically extracts a single atmospheric column from the GCM and holds the complete physical processes of the parent GCM, with model dynamics replaced by boundary forcing. As the SCM is computationally efficient and also free from complex dynamic feedback, it has been widely utilized as a testbed for developing new physical parameterizations for GCMs [49].

3.1. Single Column Model Experiments

To hint at the instantaneous differences between the two radiation schemes and to identify potential sources of divergence, we conduct GRIST-SCM experiments using BCC-RAD and RRTMG, respectively. The ARM97 and TWP06 cases from the SCM Intensive Observation Periods (IOPs) provided by the Atmospheric Radiation Measurement (ARM) program are selected [50] (available at <https://www.arm.gov> (accessed on 11 October 2023)). Observations of radiation budgets, atmospheric temperature and humidity, wind profiles, etc., are provided from ARM IOPs. This part aims to understand the differences between the two radiation schemes over mid-latitude land (with fewer clouds) and tropical ocean (with more clouds) areas, providing basic insights for subsequent global climate-scale studies.

ARM97 is located at the ARM Southern Great Plain (SGP) site (36.605° N, 97.485° W) and is deemed to represent a continental climate region with primarily stratiform clouds. Extensive measurement of temperature, relative humidity, solar radiation, etc., was conducted from 18 June to 18 July 1997. With the atmospheric profiles from ARM97 as constraints in GRIST-SCM, we simulate the period from 19 June to 28 June 1997 (a total of 10 days), with a time step of 1 h.

TWP06 is situated in the tropical coastal region of northern Australia (12.425° S, 130.891° E) and generally represents tropical marine weather systems with convective clouds. The observation period in TWP06 was from 18 January to 13 February 2006. Similar to the ARM97 case, we conduct 10-day GRIST-SCM runs for the TWP06 case from 18 January to 27 January 2006, also with a time step of 1 h. See Table 2 for details.

Table 2. Basic information about experimental configurations.

	ARM97	TWP06
Location	36.605° N, 97.485° W	12.425° S, 130.891° E
Observation period	from 18 June to 19 July 97	from 18 January to 13 February 2006
Simulation period	From 19 June to 28 June 1997	from 18 January to 27 January 2006
Time resolution		1 h
Model time step		1200 s
Vertical layer number		30

3.2. GCM Experiments

Based on the SCM experiments, we proceed with GCM experiments to reveal the impact of BCC-RAD on simulated climates.

Two groups of simulations are conducted with two different choices of moist physics in GRIST-A23.6.26. In group 1, the PhysC package [25] is utilized. Decadal climatological simulations (2011–2020) are conducted using the RRTMG and BCC-RAD schemes, respectively. The simulation with RRTMG is regarded as the control run. Though the GRIST model is capable of employing a global VR configuration, we use a quasi-uniform configuration (G6 mesh, i.e., 120 km) commonly used for AMIP-type simulations [51]. The vertical resolution is a 30-full-level Lorenz grid extending up to 2.25 hPa at the top of the atmosphere. The group 2 experiments are the same as those in group 1, but a different physics package is applied instead of that used in group 1. Basic information of the experiment is shown in Table 3.

Table 3. Basic information about experimental configurations.

	Group 1	Group 2
Physics parameterization scheme	PhysC	PhysCN
Radiation scheme		RRTMG BCC-RAD
Simulation period	2011–2020 (monthly average)	
Horizontal resolution	G6 (120 km)	
Time step	1200 s	
Vertical layer number	30	

We focus our investigation on the simulation results of radiative energy balance, distribution of clouds, and atmospheric conditions such as air temperature and relative humidity. The observational data for cloud cover, radiative fluxes, and cloud radiative forcing used here are from CERES-EBAF spanning from January 2011 to December 2020 with a spatial resolution of $1^\circ \times 1^\circ$, available at <https://ceres.larc.nasa.gov/data/> (accessed on 28 April 2022). The benchmark dataset for cloud ice content and cloud water content is from the ERA5 reanalysis monthly output, ranging from 2011 to 2020 with a spatial resolution of $1^\circ \times 1^\circ$. The CMIP6 multi-model (40 GCMs) datasets [52] are also used in our analyses.

4. Results

4.1. Comparison between BCC-RAD and RRTMG in the Single Column Model

4.1.1. ARM97

Figure 1 shows the simulated and observed atmospheric temperature, relative humidity, and distribution of cloud cover from 1000 hPa to 100 hPa. At the ARM97 site, both radiation schemes realistically reproduce the atmospheric temperature, adequately capturing the wave shape variations below 600 hPa (Figure 1a–c). The differences between the two radiation schemes and between each scheme and the observational data are generally within ± 1 K. The simulated relative humidity (RH) for both radiation schemes is consistent (Figure 1d–f) since RH primarily depends on the moist physics of the model. However, both simulations exhibit an overestimated amount of water vapor in the mid-to-upper troposphere compared with the ARM97 observation, leading to an overestimation of cloud cover (as shown in Figure 1g–i), especially high-level ice clouds.

Figure 2 shows the comparison of radiation budget at TOA and the surface. Both BCC-RAD and RRTMG capture the diurnal variation in shortwave radiation well (Figure 2a,e). Nevertheless, the net shortwave radiation fluxes at the TOA (SWNT) and the surface (SWNS) are notably smaller than the observed values for both schemes, which is probably related to the overestimated cloud cover that reflects more solar radiation to space. For longwave radiation, both schemes capture the overall trend of the TOA and surface net longwave fluxes (LWNT and LWNS, respectively) during the study period (Figure 2c,g).

but also show a systematic overestimation, especially at TOA. This is again due to the overestimated cloud cover (note that the simulated LWNT values are much closer to the observation during days 2–4 when it was mostly cloud-free). It is also seen that the LWNT from BCC-RAD is overall closer to the observation compared to RRTMG, whereas the differences in simulated LWNS between the two schemes are minimal. In general, Figure 2 indicates that the inter-scheme differences are mostly much smaller than the simulation/observation differences.

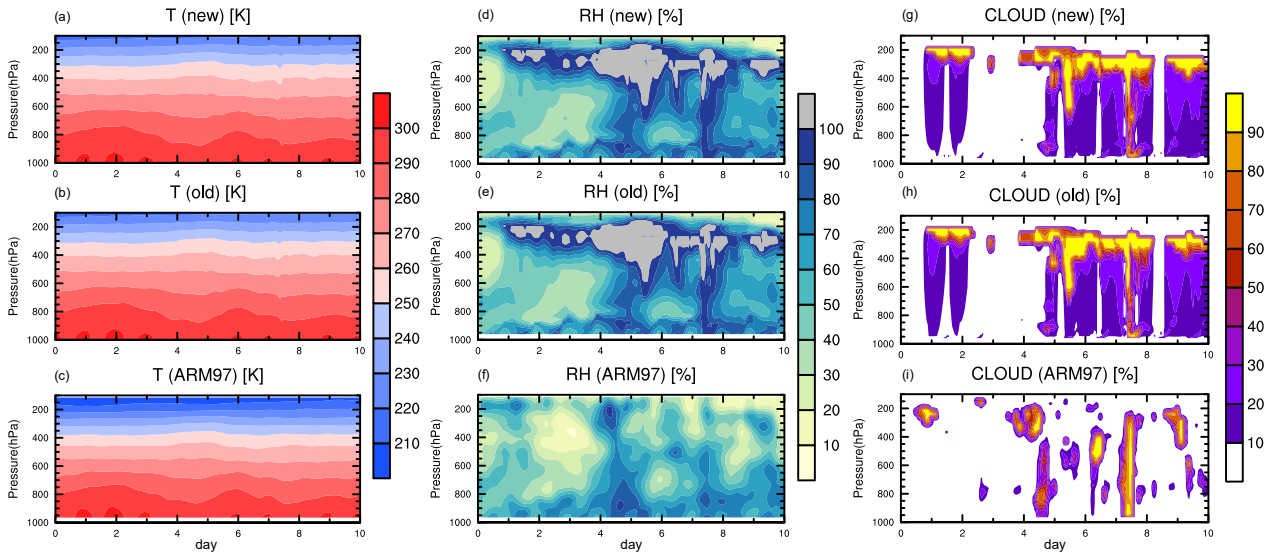


Figure 1. The atmospheric temperature (a–c), relative humidity (d–f), and cloud fraction (g–i) at the ARM97 site. Panels from top to bottom are the results of BCC-RAD, RRTMG, and the ARM97 observation.

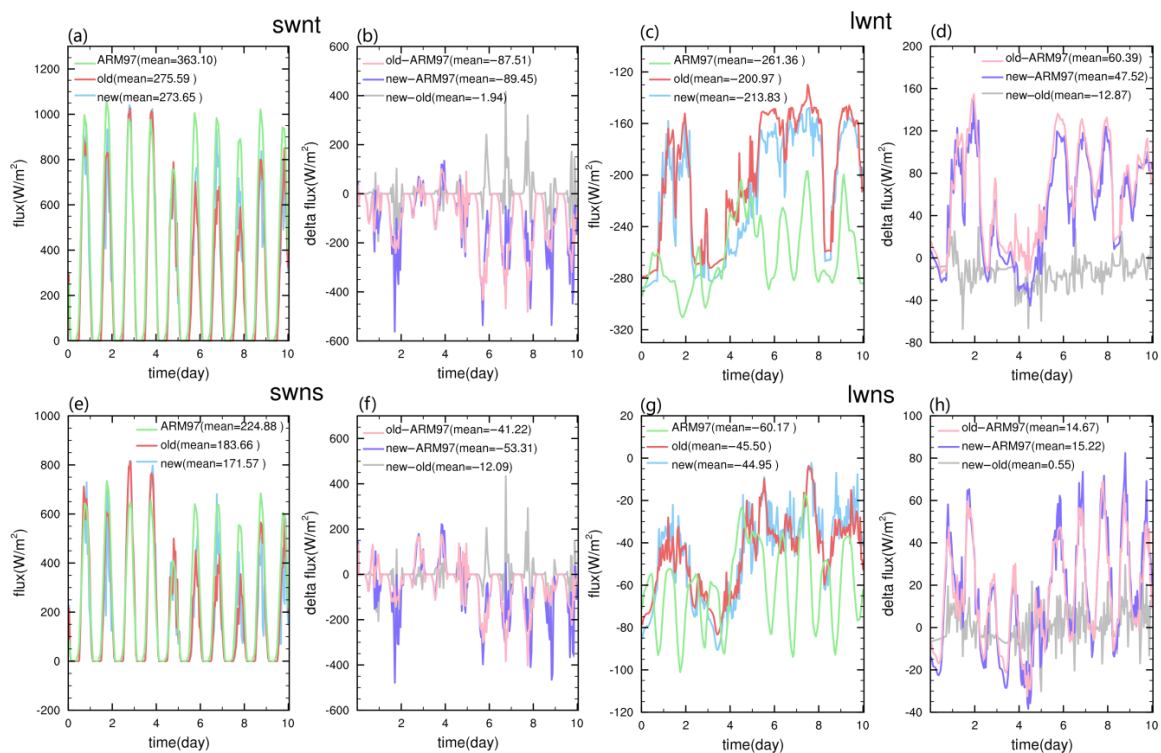


Figure 2. The diurnal variation in SWNT, LWNT, SWNS, and LWNS. (a,c,e,g) show the results of BCC-RAD, RRTMG, and ARM97. (b,d,f,h) show the differences between two schemes and between each scheme and ARM97.

To understand the sources of the inter-scheme differences, Figure 3 splits the TOA fluxes into contributions from clear-sky conditions and cloud radiative forcing. It is shown that the differences in SWNT between the two schemes are not much less significant than compared with those in LWNT. At the ARM97 site, the average difference in LWNT during the study period between BCC-RAD and RRTMG is approximately -12.9 W/m^2 , with -8.0 W/m^2 contributed from the clear-sky flux at the top of the atmosphere (i.e., LWNTC). Under clear-sky conditions, clouds are no longer the dominant factor affecting radiation flux variations, and the changes in longwave radiation flux are mainly influenced by greenhouse gases and other factors. This also indicates that in cloud-limited regions, notable differences between BCC-RAD and RRTMG may occur due to differing treatments of greenhouse gases and aerosols.

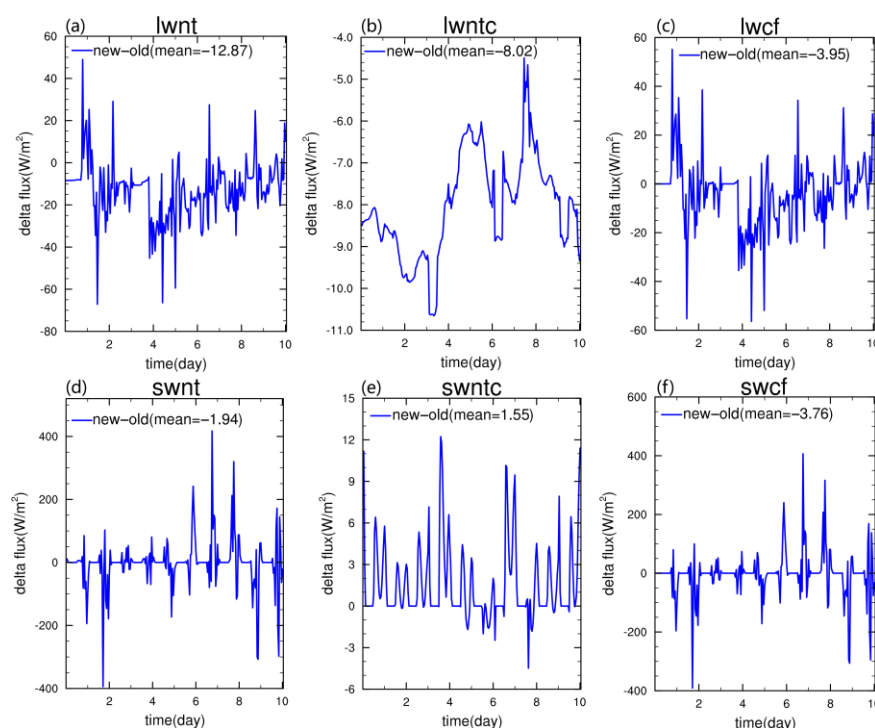


Figure 3. (a–c) represent the differences in net longwave radiation flux, net longwave radiation flux in clear sky conditions, and longwave cloud radiative forcing between BCC-RAD and RRTMG at the ARM97 site, respectively. (d–f) are similar but for shortwave radiation.

4.1.2. TWP06

The tropical ocean site TWP06 is quite similar to the ARM97 case in that the simulated atmospheric temperatures are generally close to observation (see Figure 4a–c) and there is significant overestimation of relative humidity (see Figure 4d–f) and cloud cover (see Figure 4g–i) at the upper troposphere. Nevertheless, both schemes capture the variation patterns of RH and cloud cover in the mid-troposphere well, for instance with the prevailing high-level thin clouds around 200–300 hPa during days 0–2 and the development of a deep convective system on days 6–7 (see Figure 4d–i).

For the longwave and shortwave radiation at the atmospheric top and surface (see Figure 5), the SWNT simulated by the two radiation schemes remains slightly lower compared to the observations, with the results from both schemes being very similar. Regarding the LWNT, BCC-RAD yields values even lower than those from RRTMG when compared to observations (to be explained later). At the surface, although the differences between both schemes and observed SWNS are not substantial, BCC-RAD aligns more closely to the observation. However, for the LWNS, the simulation results from both schemes are underestimated.

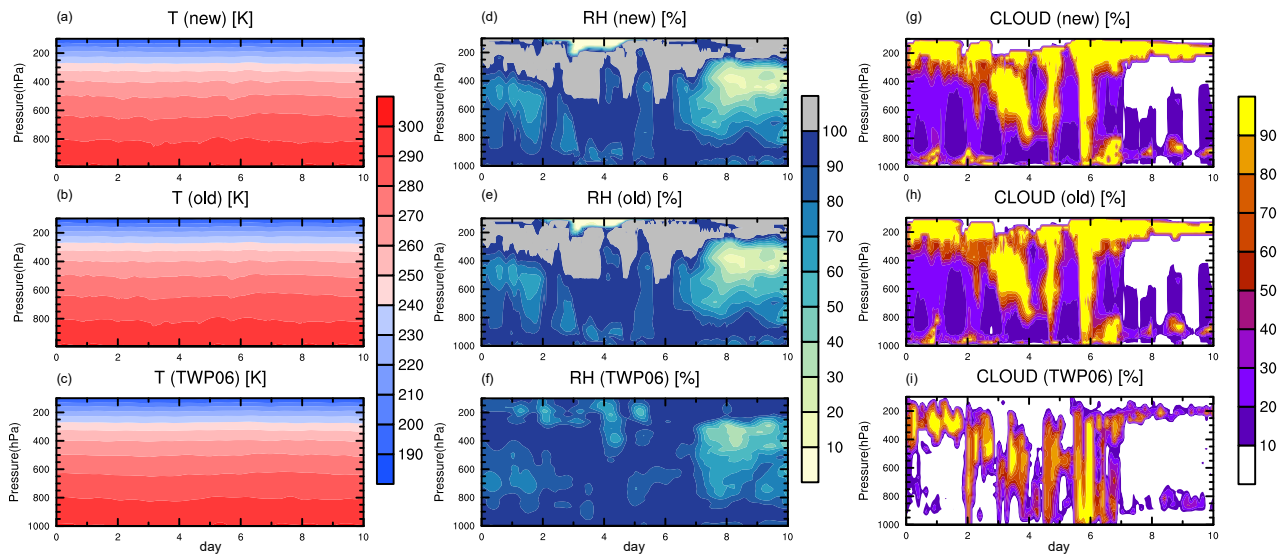


Figure 4. The atmospheric temperature (a–c), relative humidity (d–f), and cloud fraction (g–i) at the TWP06 site. Panels from top to bottom are the results of BCC-RAD, RRTMG, and the TWP06 observation.

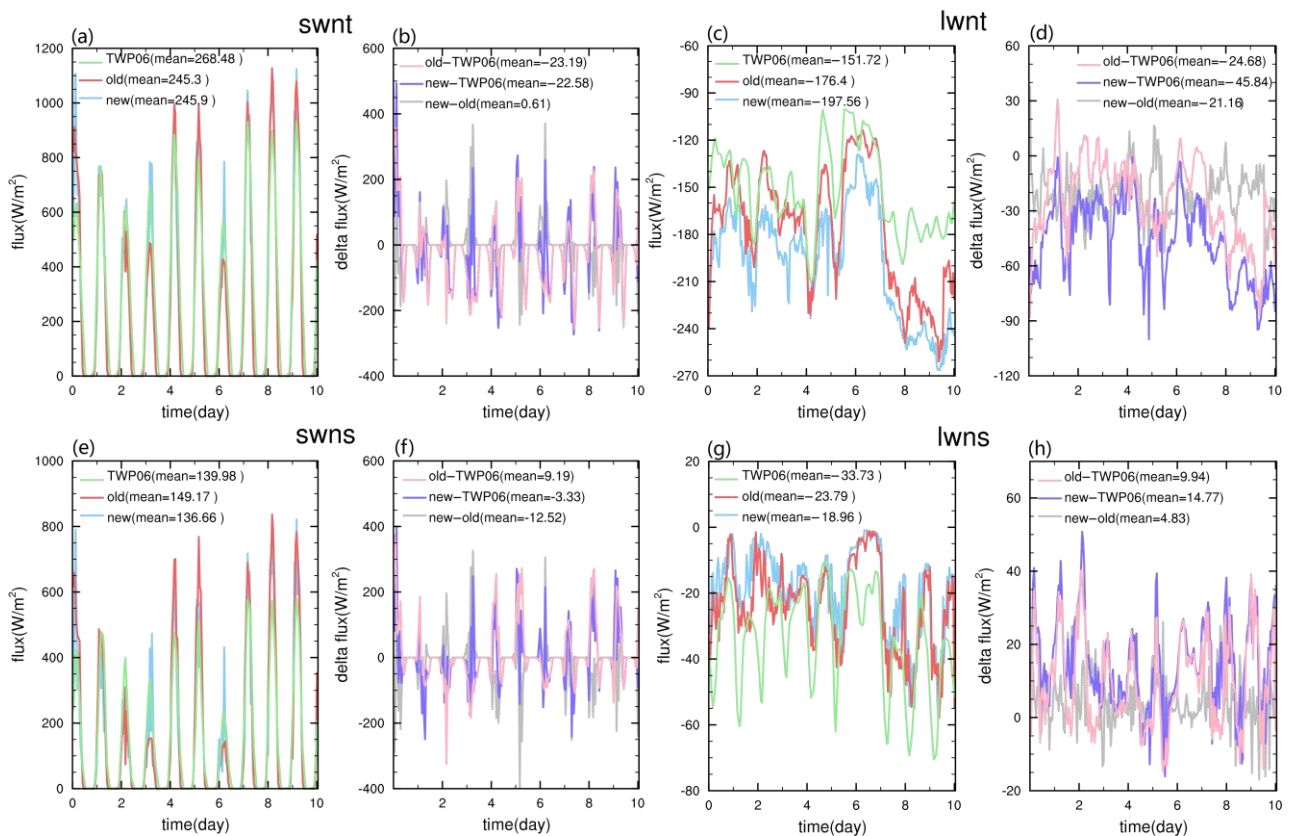


Figure 5. The diurnal variation in SWNT, LWNT, SWNS, and LWNS. (a,c,e,g) show the results of BCC-RAD, RRTMG, and TWP06. (b,d,f,h) show the differences between two schemes and between each scheme and TWP06.

Similar to the ARM97 case, the differences in the simulated LWNT between the two schemes in the TWP06 case are much larger than the differences in SWNT, as illustrated in Figure 6. The results indicate that out of the difference of -21.0 W/m^2 between BCC-RAD and RRTMG, -14.5 W/m^2 arises from the difference in LWCF. This suggests that in regions

with a prevalence of convective clouds and large cloud cover, the differing treatment of clouds (both optical properties and macro-structure) becomes a significant factor causing variations in the simulation results.

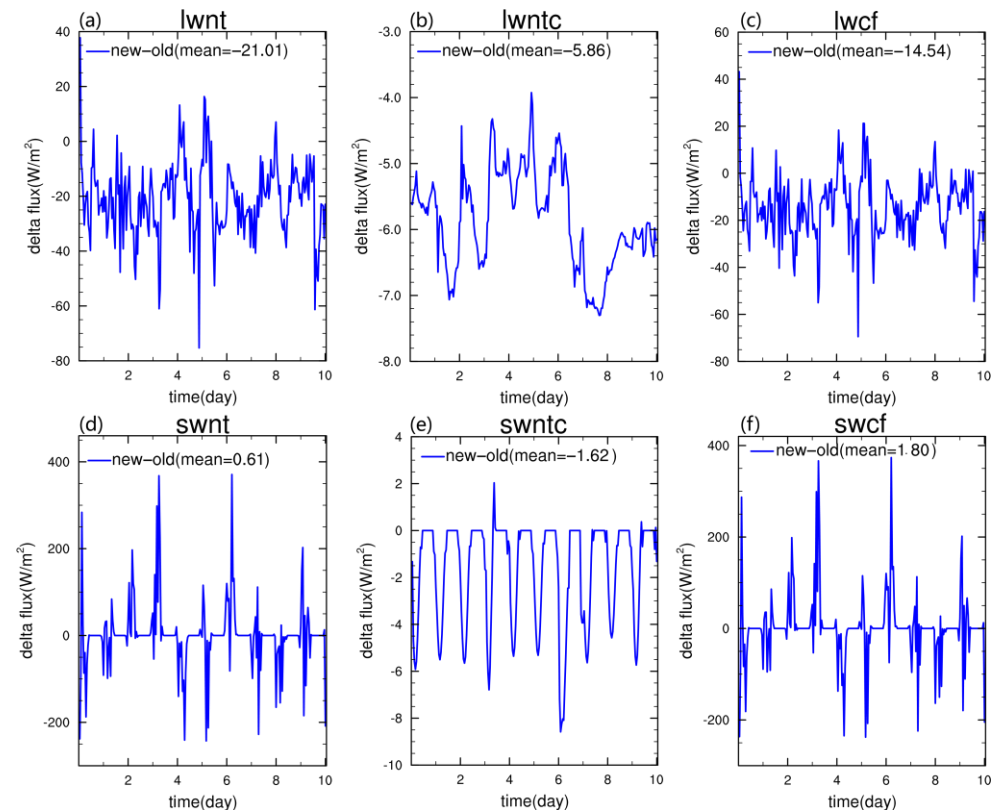


Figure 6. (a–c) represent the differences in net longwave radiation flux, net longwave radiation flux in clear sky conditions, and longwave cloud radiative forcing between BCC-RAD and RRTMG at the TWP06 site, respectively. (d–f) are similar but for shortwave radiation.

4.2. GCM Simulations under PhysC Parameterization Scheme

This section presents the GCM simulation results of the two radiation schemes under PhysC, annually averaged over the simulation period (2011–2020), to assess the impact on modeled climate by involving BCC-RAD. The GCM results under the PhysCN parameterization scheme are analyzed in the next section.

4.2.1. Global Distributions

In climate models, cloud cover is a key factor that directly affects the simulated radiation balance as well as precipitation. Figure 7 shows the distribution of total cloud cover (CLDTOT), longwave cloud forcing (LWCF), and shortwave cloud forcing (SWCF) in CERES and the biases in simulated CLDTOT, LWCF, and SWCF compared with the CERES dataset. Also shown are the differences between BCC-RAD and RRTMG. In general, the GRIST model underpredicts CLDTOT in most regions, especially in the tropics and subtropics, regardless of which radiation scheme is used. Compared with RRTMG, BCC-RAD has improved the negative CLDTOT simulation results almost globally (as shown in Figure 7d). The global mean improvement in CLDTOT is ~3% (Table 4). The improvement is more obvious in the tropical Western Pacific region and the subtropical western coasts of each continent, where GCMs share common biases. This suggests that BCC-RAD may better represent the surface–atmosphere energy interaction and consequently yield better boundary layer and convective dynamics that are key to cloud formation.

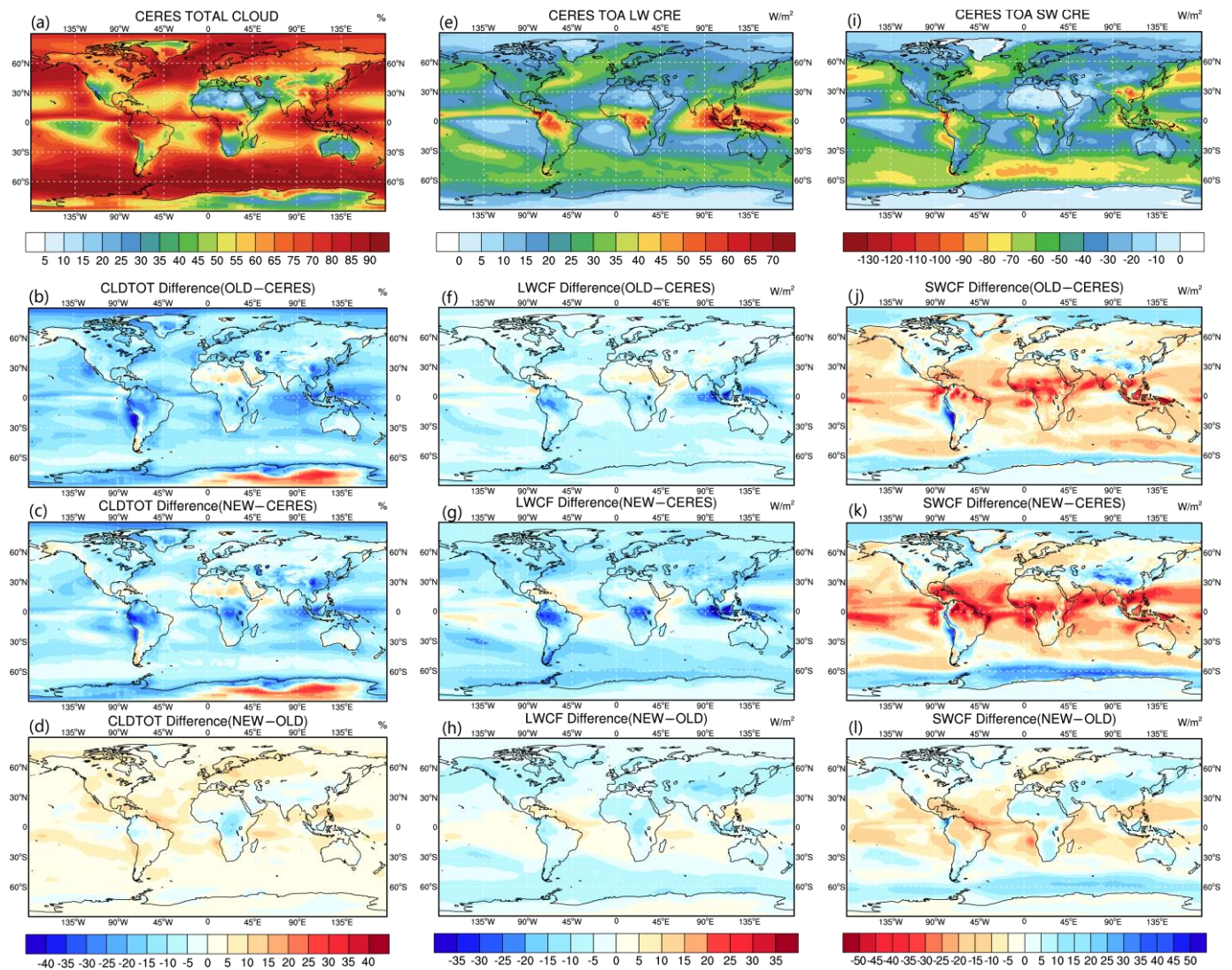


Figure 7. The distribution and bias of annual mean CLDTOT, LWCF, and SWCF under PhysC. (a–d) are CLDTOT distribution of observation, the differences between RRTMG and CERES, BCC-RAD, and CERES, and two radiation schemes, respectively. (e–h) and (i–l) are the same, but for LWCF and SWCF, respectively.

The models also show considerable biases in simulated LWCF (Figure 7f–h) and SWCF (Figure 7j–l) compared to the CERES observations. There is an overall underestimation of LWCF and an overestimation (underestimation) of SWCF in tropical convective zones (high-latitude oceans) regardless of radiation schemes. By using BCC-RAD, the negative LWCF biases are slightly reduced over parts of the tropical oceans but are enhanced in other locations such as the tropical convective cores, resulting in a $\sim 3 \text{ W/m}^{-2}$ reduction in LWCF from ~ -19.4 to $\sim -16.4 \text{ W/m}^{-2}$ (see Table 4). For SWCF, BCC-RAD reduces the positive (negative) biases over the subtropical western coasts of North and South America (the mid-latitude Northern Pacific Ocean) but enlarges the negative (positive) biases over the tropics (the Southern Ocean). The overall decreases in LWCF and SWCF by BCC-RAD in the GRIST model are comparable to the results of its application in the BCC_AGCM2.0.1 model [10], but with different distributions. In general, the overall improvement in cloud cover as stated above by using BCC-RAD does not bring corresponding improvement in cloud radiative forcings. This is most likely due to the very different representations of cloud particle optics as well as the vertical overlap between the two schemes. Nevertheless, the physics parameterizations also play a large role in modulating the simulated clouds;

for instance, PhysC significantly underpredicts ice cloud content (see Table 4), which could explain to a large extent the significant underestimation of LWCF. When we shift to PhysCN, the biases in both ice cloud content and cloud radiative forcings decline greatly (see Section 4.3).

Table 4. The table presents the global annual mean values of radiation-related variables from different radiation schemes and physics parameterization schemes in GRIST, as well as reference data from CERES, ERA5, and CMIP6 datasets.

Variable Name ¹	RRTMG (PhysC)	BCC-RAD (PhysC)	RRTMG (PhysCN)	BCC-RAD (PhysCN)	OBS	CMIP6
CLDTOT (%)	55.30	58.33	59.84	62.18	67.37	63.96
SWCF (W/m^{-2})	−52.70	−54.07	−42.04	−39.17	−45.11	−47.80
LWCF (W/m^{-2})	19.41	16.38	23.28	23.79	25.61	24.10
FSWT (W/m^{-2})	236.61	238.44	247.41	253.75	240.47	−239.50
FSWTC (W/m^{-2})	289.34	292.51	289.48	292.93	286.81	287.30
FLWT (W/m^{-2})	−241.00	−249.53	−238.51	−245.33	239.24	238.30
FLWTC (W/m^{-2})	−260.42	−266.09	−261.79	−269.30	−266.08	−262.40
TOA NET (W/m^{-2})	−4.40	−11.09	8.90	8.42	1.23	−5.50
FSWS (W/m^{-2})	161.82	161.21	173.06	174.08	164.24	163.40
FSWSC (W/m^{-2})	219.13	220.95	218.93	220.63	212.10	214.60
FLWS (W/m^{-2})	−51.63	−57.71	−54.65	−57.84	−53.92	−56.20
FLWSC (W/m^{-2})	−78.10	−86.05	−77.50	−84.51	−81.12	−81.70
SFC NET (W/m^{-2})	110.19	103.50	118.41	116.24	110.32	107.20
IWC (mg/kg)	0.73	0.75	(5.92) ³	(5.84) ³	1.55 ² (4.46) ^{2,3}	-
LWC (mg/kg)	5.40	5.62	4.52	4.79	4.37 ²	-
SFC TEMP (K)	288.40	287.82	288.84	288.68	279.35 ²	-
PRECT (mm)	3.11	3.13	2.92	2.92	2.44 ²	-

¹ CLDTOT, total cloud cover; SWCF, shortwave cloud forcing; LWCF, longwave cloud forcing; FSWT, shortwave radiation flux at TOA; FSWTC, shortwave radiation flux at TOA in clear-sky conditions; FLWT, longwave radiation flux at TOA; FLWTC, longwave radiation flux at TOA in clear-sky conditions; TOA NET, net radiation flux at TOA; FSWS, shortwave radiation flux at surface; FSWSC, shortwave radiation flux at surface in clear-sky conditions; FLWS, longwave radiation flux at surface; FLWSC, longwave radiation flux at surface in clear-sky conditions; SFC NET, net radiation flux at surface; IWC, ice water content; LWC, liquid water content; SFC TEMP, surface temperature; PRECT, total precipitation. ² The reference data of IWC, LWC, SFC TEMP, and PRECT are from ERA5. Others are from CERES. ³ The SI microphysics used in PhysCN do not distinguish cloud ice from snow, which results in high IWC values in simulation. The ERA5 reference in “()” is the sum of IWC and snow content.

The comparisons of the global distribution of surface pressure and surface temperature are shown in Figure 8. It is seen that the differences in surface pressure between the two radiation schemes and between each radiation scheme and CERES observations are not significant. The discrepancies between BCC-RAD and RRTMG are generally within ± 4 hPa. It is noted that BCC-RAD exhibits slight improvements (reducing the negative biases) compared to RRTMG in many regions, such as nearly all land areas and certain marine regions. For surface temperature, BCC-RAD improves the negative bias of RRTMG in most Southern hemisphere ocean regions and the positive bias of most land areas to some extent, but expands the negative bias of RRTMG in northern Eurasia and the land regions at the poles.

The global means of the simulation results of the two radiation schemes under both PhysC and PhysCN parameterization schemes are shown in Table 4. Also shown are the corresponding observations and multi-model means from the CMIP6 datasets. It can be observed that under PhysC, the global CLDTOT simulated by BCC-RAD is closer to the CERES observations as well as the CMIP6 results compared to RRTMG. This is consistent with what is shown in Figure 7a–d. In terms of the TOA net radiation balance (TOT NET), however, RRTMG is closer to the CERES observations as well as CMIP6 under PhysC. As aforementioned, this is partly due to the discrepancies in cloud radiative forcing, especially in LWCF, and partly due to the differences in clear-sky fluxes (FLWTC and FSWTC). It should be noted that the simulated LWCFs by RRTMG and BCC-RAD differ

from the CERES observation ($\sim -25.6 \text{ W/m}^2$) by as large as 6.2 W/m^2 and 9.2 W/m^2 , respectively. Since cloud radiative forcing is a significant contributor to the net radiation flux, such large deviations in LWCF can lead to substantial errors in the net radiation balance. That considered, the relatively small bias in TOT NET by RRTMG may be a result of compensating errors that cancel each other out. Note that the FLWTC from BCC-RAD is nearly identical to the CERES observations, but that from RRTMG is almost 6 W/m^2 smaller than the observation.

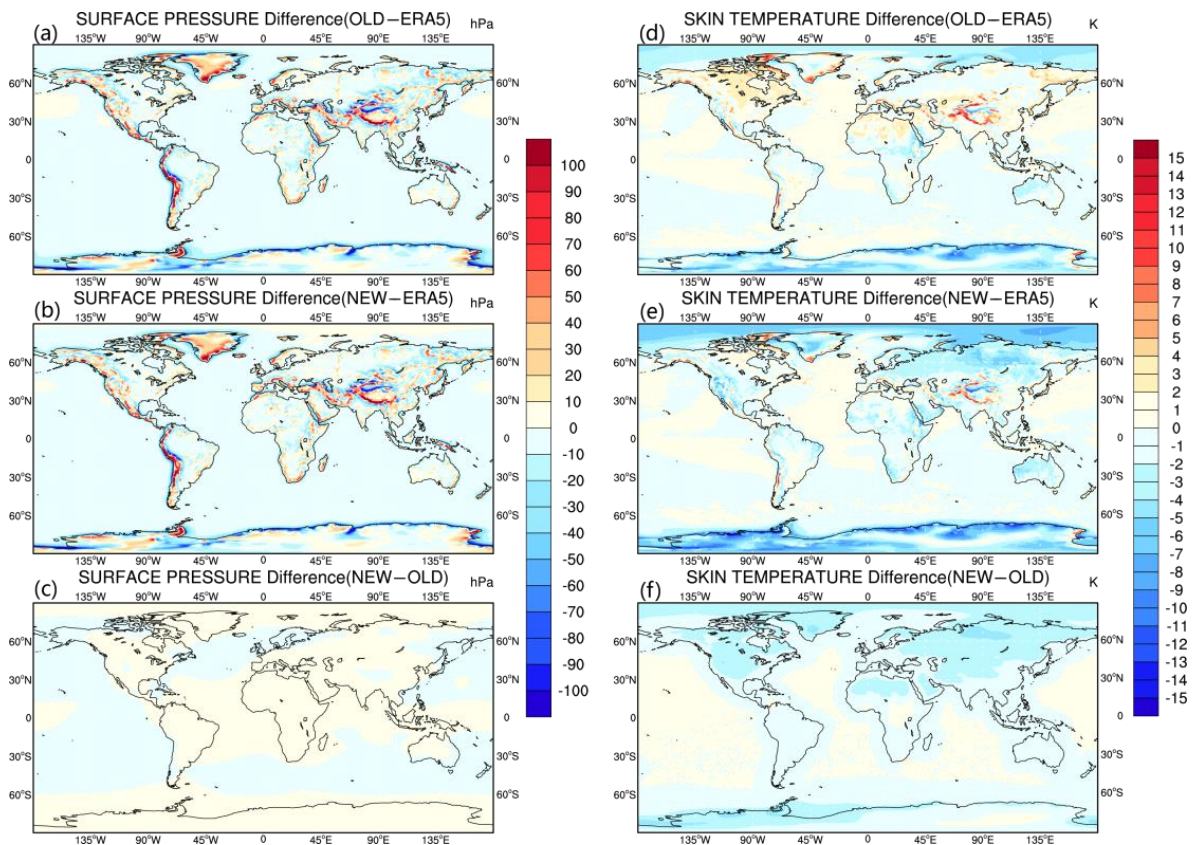


Figure 8. (a–c) displays the distribution difference plots of annual mean surface pressure under PhysC. (d–f) is similar to (a–c) but for surface temperature.

4.2.2. Atmospheric State

Atmospheric temperature (T) and relative humidity (RH) play a crucial role in cloud formation and radiation transmission, as well as the behavior of water vapor in the atmosphere. Examining T and RH provides insights into the underlying physical processes that govern radiation interactions within the atmosphere.

This section analyzes the vertical structure of the simulated T and RH under PhysC. Figure 9 shows the mean zonal-height of T (Figure 9a–f) and RH (Figure 9g–l). Simulations with both radiation schemes are able to capture the main features of the vertical structure of T and RH from the ERA5 reanalysis. However, the model tends to overestimate T in the Southern hemisphere troposphere and the tropical tropopause (Figure 9d,e) by at most $>13 \text{ K}$. BCC-RAD has to some extent diminished the high-temperature biases, particularly around 200 hPa in low latitudes with a maximum decrease of approximately -4.0 K . A similar decrease in temperature around 200 hPa was also found by Zhang et al. [10]. Moreover, the simulated relative humidity by BCC-RAD has also shown some improvement compared to RRTMG (Figure 9j–l). For instance, it significantly reduces the positive biases at high altitudes in low and high latitudes and brings the negative biases in the mid-latitude Southern hemisphere closer to zero.

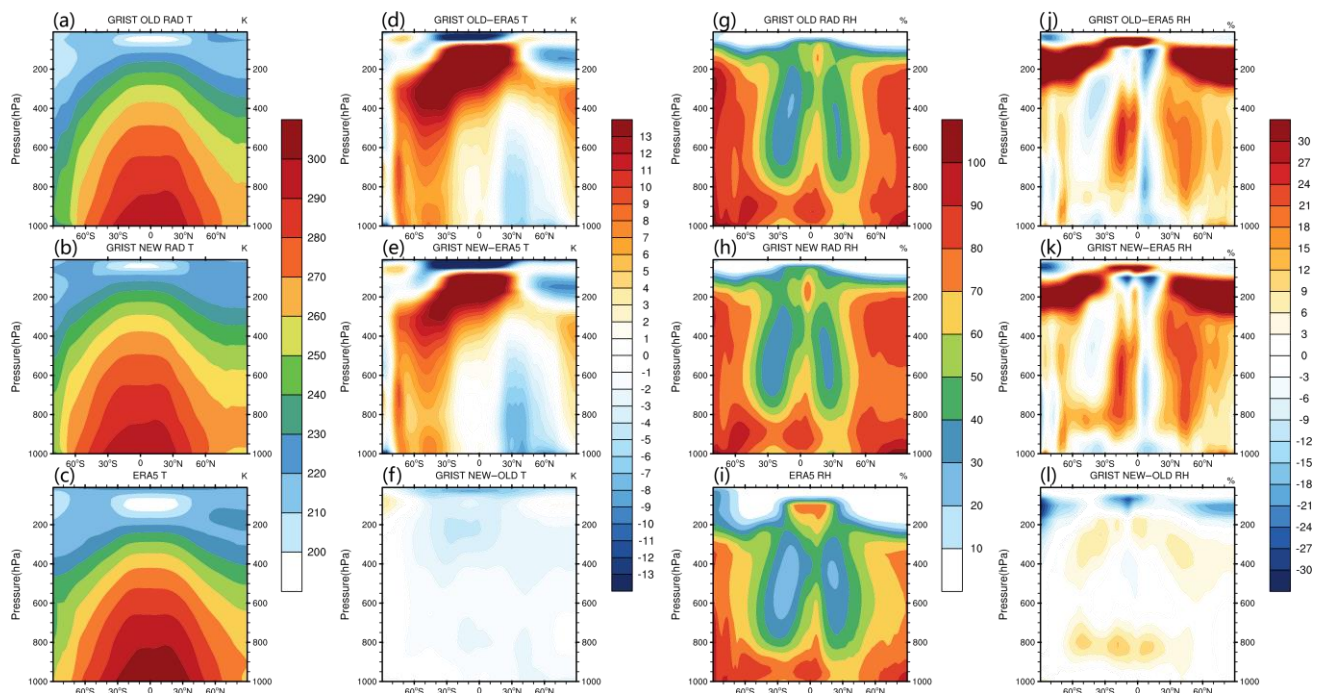


Figure 9. The annual mean zonal-height distribution and bias of T and RH in atmosphere under PhysC. (a–c) represents the zonal-height distribution of T in RRTMG, BCC-RAD, and ERA5. (d–f) shows the difference of T between RRTMG and ERA5, BCC-RAD and ERA5, and BCC-RAD and RRTMG. (g–i) and (j–l) are the same as (a–c) and (d–f), respectively, but for RH.

4.3. GCM Simulations under the PhysCN Parameterization Scheme

The above results hint that cloud microphysics may have profoundly influenced the cloud properties (e.g., cloud ice/water content) and hence the radiative budgets simulated by GRIST. In that sense, it is warranted to evaluate the impact of BCC-RAD under a different microphysics configuration. In this section, we analyze the performance of BCC-RAD and RRTMG under the alternative PhysCN physics (described in Section 3.2).

4.3.1. Global Distributions

Similar to Figure 7, Figure 10 provides the comparisons of CLDTOT, LWCF, and SWCF for the experiments with PhysCN. The comparison between Figures 7 and 10 reveals a notable reduction in the model/observation discrepancies in CLDTOT and LWCF in oceanic regions by shifting to the PhysCN parameterization scheme. The global mean LWCF is now much closer to the CERES observation ($\sim -25.6 \text{ W/m}^2$) for both radiation schemes (~ -23.3 and -23.8 W/m^2 for RRTMG and BCC-RAD, respectively). However, a substantial overestimation of LWCF is seen in the tropical equatorial region, especially the equatorial Pacific region (Figure 10d–e). This is probably because the PhysCN parameterizations intensify the tropical convection and the upper-level cloud ice content. Nevertheless, the positive LWCF forcing is apparently smaller for BCC-RAD than for RRTMG. As for the SWCF, the use of PhysCN effectively rectifies the previously significant underestimation in the vast low–middle latitudes. Compared to RRTMG, BCC-RAD exhibits notable improvement in SWCF in the equatorial West Pacific and near the western coast of North and South America.

The inclusion of PhysCN has significantly improved the simulated CLDTOT and LWCF (see Table 4). The LWCF biases compared to CERES of RRTMG and BCC-RAD are reduced, respectively. Similarly, the biases in CLDTOT decreased from 12.07% and 9.04% W/m^2 to 7.53% W/m^2 and 5.19% for RRTMG and BCC-RAD, respectively. Both the global distributions and the global mean results demonstrate that, under the PhysCN

parameterization scheme, BCC-RAD outperforms RRTMG in simulating various variables both regionally and globally.

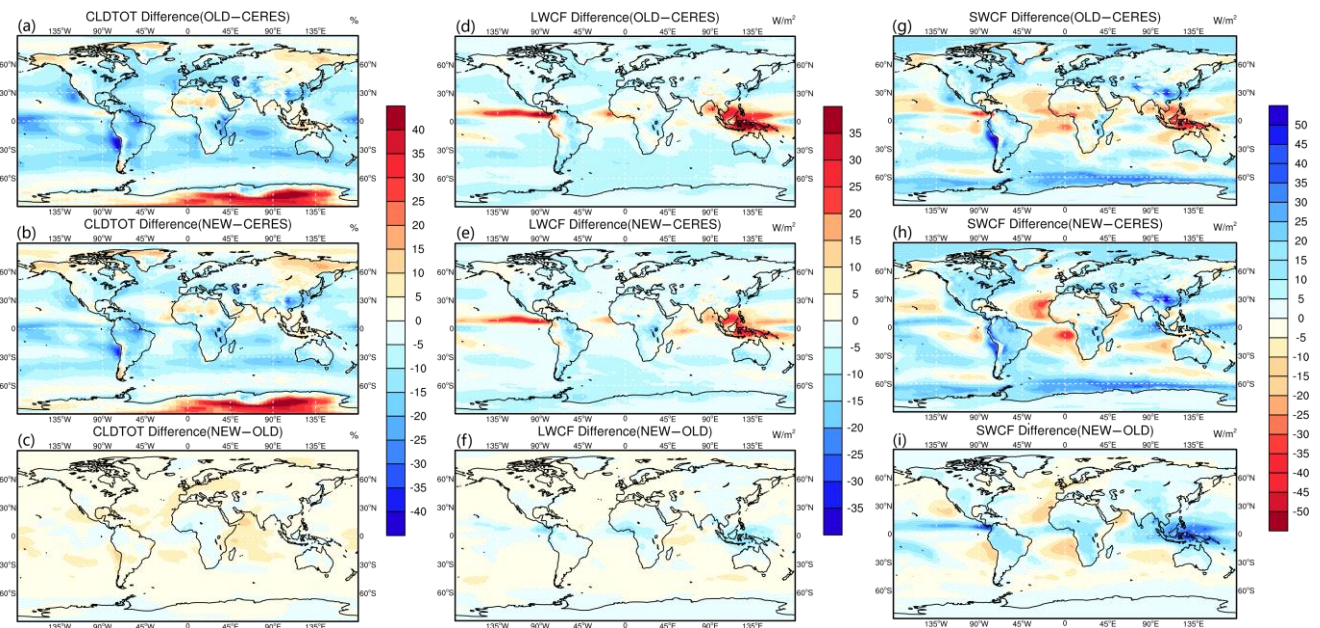


Figure 10. The distribution and bias of annual mean CLDTOT, LWCF, and SWCF under PhysCN. (a–c) are CLDTOT distribution of the differences between RRTMG and CERES, BCC-RAD, and CERES, and two radiation schemes, respectively. (d–f) and (g–i) are the same, but for LWCF and SWCF, respectively.

The global distributions of the simulated surface pressure and temperature under PhysCN generally mimic the results under PhysC (see Figure 11).

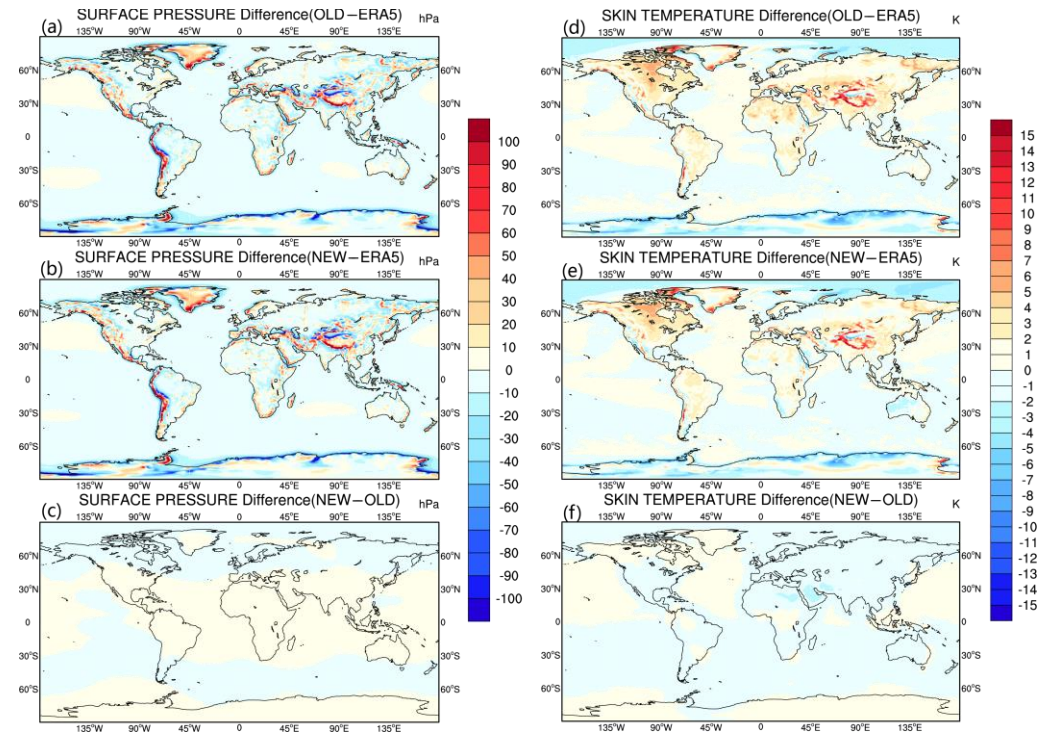


Figure 11. (a–c) displays the distribution difference plots of annual mean surface pressure under PhysCN. (d–f) is similar to (a–c) but for surface temperature.

4.3.2. Atmospheric State

Figure 12 shows the modeled atmospheric temperature and relative humidity, as well as the discrepancies compared to the ERA5 reanalysis. It is seen by comparing with Figure 10 that the patterns of the model/reanalysis discrepancies largely persist in Figure 12. Nevertheless, considering the differences between the two radiation schemes, BCC-RAD provides better atmospheric temperature and relative humidity in the mid-to-lower troposphere around 30° N, which is advantageous for subsequent research in the East Asian region. Actually, BCC-RAD effectively addresses the issue of excessive relative humidity in the mid-to-lower troposphere at nearly all latitudes. Its simulation of the mid-latitude troposphere relative humidity in the Southern Hemisphere, as well as the patterns in the troposphere at the equator and in the middle latitudes of the Northern Hemisphere, also aligns more closely with the observations.

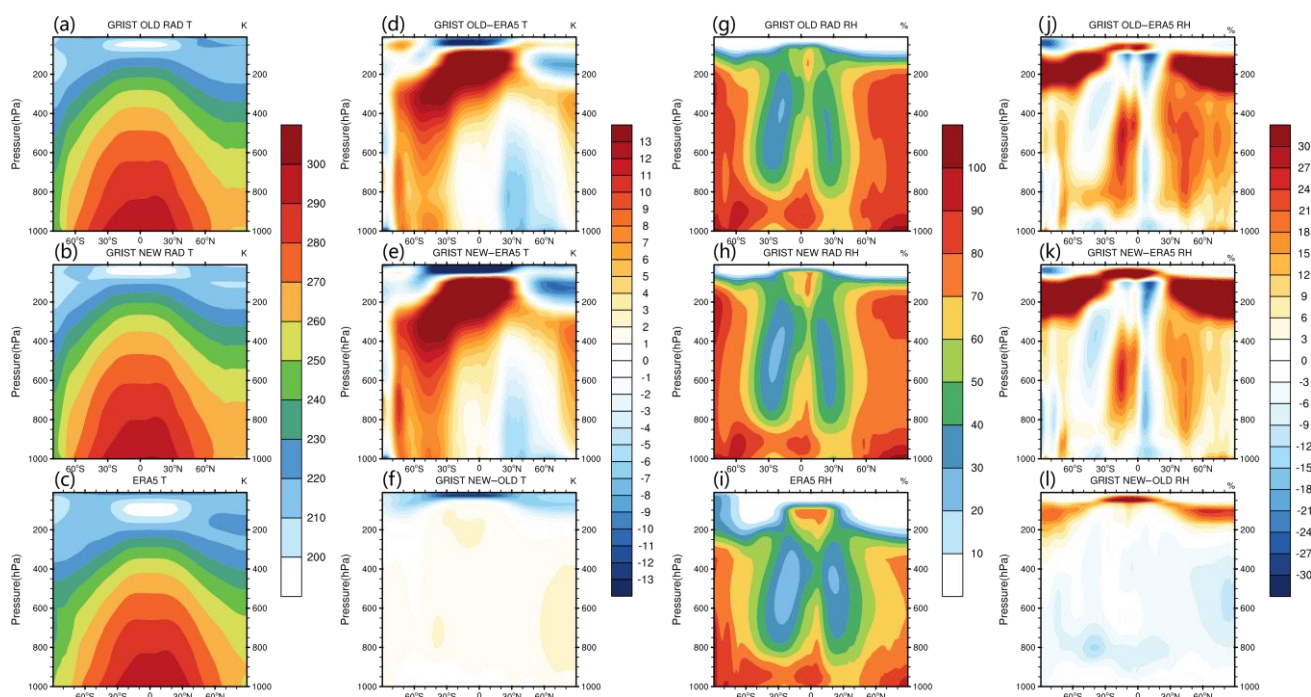


Figure 12. The annual mean zonal-height distribution and bias of T and RH in atmosphere under PhysCN. (a–c) represents the zonal-height distribution of T in RRTMG, BCC-RAD, and ERA5. (d–f) shows the difference of T between RRTMG and ERA5, BCC-RAD and ERA5, and BCC-RAD and RRTMG. (g–i) and (j–l) are the same as (a–c) and (d–f), respectively, but for RH.

5. Conclusions and Discussion

In this study, we incorporated the BCC-RAD radiation scheme, which is potentially more suitable for a variable-resolution model framework, into the GRIST model and documented its impact on simulated climate in comparison with the original RRTMG scheme.

The results from SCM tests with two distinct cases demonstrate that BCC-RAD is able to produce very similar atmospheric states and cloud distributions compared to RRTMG. Meanwhile, notable differences in radiation fluxes are also seen for clear-sky longwave radiation and cloud radiative forcing. These differences indicate the differing treatments of greenhouse gas absorption and cloud optical properties between the two schemes, which could influence the simulated climate in full GCM simulations.

GCM climate experiments are conducted with the two radiation schemes under two physics parameterization packages. The results indicate that, when using the PhysC scheme, BCC-RAD significantly improves the simulation of cloud cover (by ~3%). The simulated atmospheric temperature and relative humidity also more closely resemble the observations, particularly above 200 hPa.

When utilizing the PhysCN parameterization package, convection is enhanced and cloud ice content increases by ~8 times to a more reasonable level. The simulation of cloud cover and cloud radiative forcing for both radiation schemes is greatly improved. This is consistent with the findings of Li et al. [15]. BCC-RAD outperforms RRTMG under the PhysCN physics scheme in various aspects. For instance, BCC-RAD significantly reduces the biases in cloud cover and LWCF in the tropical convective zones and also notably improves the vertical structure of temperature and atmospheric humidity.

The above results suggest that the BCC-RAD radiation scheme is able to be applied in the configuration of GRIST for global climate simulations, especially jointly used with the PhysCN physics scheme.

This study represents the first attempt to apply the BCC-RAD radiation scheme to the weather/climate-integrated GRIST model and investigate the climatic capabilities of BCC-RAD within the new model framework. The results are valuable for the future development of GRIST and other similar models. In the future, it is warranted to explore the capability of BCC-RAD in regional weather/climate simulations with the variable resolution framework of GRIST.

Author Contributions: Conceptualization, C.Y. and X.J.; methodology, C.Y., X.J., X.L., H.Z. and S.Z.; resources, X.L.; formal analysis, C.Y.; writing—original draft preparation, C.Y.; writing—review and editing, X.J., H.Z. and X.L.; visualization, C.Y.; supervision, H.Z. and S.Z. All authors have read and agreed to the published version of the manuscript.

Funding: This work was supported by the Meteorological Joined Fund by NSF and CMA (U2342224) and the Open Grants of the State Key Laboratory of Severe Weather (2022LASW-B02).

Institutional Review Board Statement: The study did not require ethical approval.

Informed Consent Statement: Not applicable.

Data Availability Statement: The raw data supporting the conclusions of this article will be made available by the authors on request. The data are not publicly available due to file sizes.

Conflicts of Interest: The authors declare no conflict of interest.

References

1. Kahn, R.A. Reducing the Uncertainties in Direct Aerosol Radiative Forcing. *Surv. Geophys.* **2012**, *33*, 701–721. [[CrossRef](#)]
2. Pincus, R.; Forster, P.M.; Stevens, B. The Radiative Forcing Model Intercomparison Project (RFMIP): Experimental protocol for CMIP6. *Geosci. Model. Dev.* **2016**, *9*, 3447–3460. [[CrossRef](#)]
3. Jahangir, E.; Libois, Q.; Couvreur, F.; Vié, B.; Saint-Martin, D. Uncertainty of SW Cloud Radiative Effect in Atmospheric Models Due to the Parameterization of Liquid Cloud Optical Properties. *J. Adv. Model. Earth Syst.* **2021**, *13*, e2021MS002742. [[CrossRef](#)]
4. Adams, S.V.; Ford, R.W.; Hambley, M.; Hobson, J.M.; Kavčič, I.; Maynard, C.M.; Melvin, T.; Müller, E.H.; Mullerworth, S.; Porter, A.R.; et al. LFRic: Meeting the challenges of scalability and performance portability in Weather and Climate models. *J. Parallel Distrib. Comput.* **2019**, *132*, 383–396. [[CrossRef](#)]
5. Giorgetta, M.A.; Brokopf, R.; Crueger, T.; Esch, M.; Fiedler, S.; Helmert, J.; Hohenegger, C.; Kornblueh, L.; Köhler, M.; Manzini, E.; et al. ICON-A, the Atmosphere Component of the ICON Earth System Model: I. Model Description. *J. Adv. Model. Earth Syst.* **2018**, *10*, 1613–1637. [[CrossRef](#)]
6. Crueger, T.; Giorgetta, M.A.; Brokopf, R.; Esch, M.; Fiedler, S.; Hohenegger, C.; Kornblueh, L.; Mauritsen, T.; Nam, C.; Naumann, A.K.; et al. ICON-A, The Atmosphere Component of the ICON Earth System Model: II. Model Evaluation. *J. Adv. Model. Earth Syst.* **2018**, *10*, 1638–1662. [[CrossRef](#)]
7. Tomita, H.; Miura, H.; Iga, S.; Nasuno, T.; Satoh, M. A global cloud-resolving simulation: Preliminary results from an aqua planet experiment. *Geophys. Res. Lett.* **2005**, *32*, 8. [[CrossRef](#)]
8. Zhang, Y.; Li, X.; Liu, Z.; Rong, X.; Li, J.; Zhou, Y.; Chen, S. Resolution Sensitivity of the GRIST Nonhydrostatic Model from 120 to 5 km (3.75 km) During the DYAMOND Winter. *Earth Space Sci.* **2022**, *9*, e2022EA002401. [[CrossRef](#)]
9. Zhang, H.; Shi, G.; Nakajima, T.; Suzuki, T. The effects of the choice of the k-interval number on radiative calculations. *J. Quant. Spectrosc. Radiat. Transf.* **2006**, *98*, 31–43. [[CrossRef](#)]
10. Zhang, H.; Jing, X.; Li, J. Application and evaluation of a new radiation code under McICA scheme in BCC_AGCM2.0.1. *Geosci. Model. Dev.* **2014**, *7*, 737–754. [[CrossRef](#)]
11. Zhang, H.; Zhu, S.; Zhao, S.; Wei, X. Establishment of high-resolution aerosol parameterization and its influence on radiation calculations. *J. Quant. Spectrosc. Radiat. Transf.* **2020**, *243*, 106802. [[CrossRef](#)]

12. Zhou, C.; Zhang, H.; Zhao, S.; Li, J. On Effective Radiative Forcing of Partial Internally and Externally Mixed Aerosols and Their Effects on Global Climate. *J. Geophys. Res. Atmos.* **2018**, *123*, 401–423. [[CrossRef](#)]
13. Zhang, H.; Zhou, C.; Zhao, S. Influences of the Internal Mixing of Anthropogenic Aerosols on Global Aridity Change. *J. Meteorol. Res.* **2018**, *32*, 723–733. [[CrossRef](#)]
14. Zhang, H.; Wang, Z.; Zhang, F.; Jing, X. Impact of four-stream radiative transfer algorithm on aerosol direct radiative effect and forcing. *Int. J. Climatol.* **2015**, *35*, 4318–4328. [[CrossRef](#)]
15. Li, X.; Zhang, Y.; Lin, Y.; Peng, X.; Li, J. Implementation of a moist physics parameterization package in the GRIST global model and its impact on the modeled climate. *Acta Meteorol. Sin.* **2023**, *81*, 630–644.
16. Chu, W.; Lin, Y.; Zhao, M. Implementation and Evaluation of a Double-Plume Convective Parameterization in NCAR CAM5. *J. Clim.* **2022**, *35*, 617–637. [[CrossRef](#)]
17. Qin, Y.; Lin, Y.; Xu, S.; Ma, H.-Y.; Xie, S. A Diagnostic PDF Cloud Scheme to Improve Subtropical Low Clouds in NCAR Community Atmosphere Model (CAM5). *J. Adv. Model. Earth Syst.* **2018**, *10*, 320–341. [[CrossRef](#)]
18. Zhao, X.; Lin, Y.; Peng, Y.; Wang, B.; Morrison, H.; Gettelman, A. A single ice approach using varying ice particle properties in global climate model microphysics. *J. Adv. Model. Earth Syst.* **2017**, *9*, 2138–2157. [[CrossRef](#)]
19. Li, X.; Zhang, Y.; Peng, X.; Chu, W.; Lin, Y.; Li, J. Improved Climate Simulation by Using a Double-Plume Convection Scheme in a Global Model. *J. Geophys. Res. Atmos.* **2022**, *127*, e2021JD036069. [[CrossRef](#)]
20. Li, J.; Zhang, Y. Enhancing the stability of a global model by using an adaptively implicit vertical moist transport scheme. *Meteorol. Atmos. Phys.* **2022**, *134*, 55. [[CrossRef](#)]
21. Wang, L.; Zhang, Y.; Li, J.; Liu, Z.; Zhou, Y. Understanding the Performance of an Unstructured-Mesh Global Shallow Water Model on Kinetic Energy Spectra and Nonlinear Vorticity Dynamics. *J. Meteorol. Res.* **2019**, *33*, 1075–1097. [[CrossRef](#)]
22. Zhang, Y.; Li, J.; Yu, R.; Zhang, S.; Liu, Z.; Huang, J.; Zhou, Y. A Layer-Averaged Nonhydrostatic Dynamical Framework on an Unstructured Mesh for Global and Regional Atmospheric Modeling: Model Description, Baseline Evaluation, and Sensitivity Exploration. *J. Adv. Model. Earth Syst.* **2019**, *11*, 1685–1714. [[CrossRef](#)]
23. Ringler, T.; Ju, L.; Gunzburger, M. A multiresolution method for climate system modeling: Application of spherical centroidal Voronoi tessellations. *Ocean Dyn.* **2008**, *58*, 475–498. [[CrossRef](#)]
24. Jacobsen, D.W.; Gunzburger, M.; Ringler, T.; Burkardt, J.; Peterson, J. Parallel algorithms for planar and spherical Delaunay construction with an application to centroidal Voronoi tessellations. *Geosci. Model. Dev.* **2013**, *6*, 1353–1365. [[CrossRef](#)]
25. Li, X.; Zhang, Y.; Peng, X.; Li, J. Using a single column model (SGRIST1.0) for connecting model physics and dynamics in the Global-to-Regional Integrated forecast SysTem (GRIST-A20.8). *Geosci. Model. Dev. Discuss.* **2020**, *2020*, 1–28.
26. Neale, R.B.; Richter, J.H.; Jochum, M. The Impact of Convection on ENSO: From a Delayed Oscillator to a Series of Events. *J. Clim.* **2008**, *21*, 5904–5924. [[CrossRef](#)]
27. Zhang, G.J.; McFarlane, N.A. Sensitivity of climate simulations to the parameterization of cumulus convection in the Canadian climate centre general circulation model. *Atmos.-Ocean* **1995**, *33*, 407–446. [[CrossRef](#)]
28. Park, S.; Bretherton, C.S. The University of Washington Shallow Convection and Moist Turbulence Schemes and Their Impact on Climate Simulations with the Community Atmosphere Model. *J. Clim.* **2009**, *22*, 3449–3469. [[CrossRef](#)]
29. Morrison, H.; Gettelman, A. A New Two-Moment Bulk Stratiform Cloud Microphysics Scheme in the Community Atmosphere Model, Version 3 (CAM3). Part I: Description and Numerical Tests. *J. Clim.* **2008**, *21*, 3642–3659. [[CrossRef](#)]
30. Mlawer, E.J.; Taubman, S.J.; Brown, P.D.; Iacono, M.J.; Clough, S.A. Radiative transfer for inhomogeneous atmospheres: RRTM, a validated correlated-k model for the longwave. *J. Geophys. Res. Atmos.* **1997**, *102*, 16663–16682. [[CrossRef](#)]
31. Iacono, M.J.; Delamere, J.S.; Mlawer, E.J.; Shephard, M.W.; Clough, S.A.; Collins, W.D. Radiative forcing by long-lived greenhouse gases: Calculations with the AER radiative transfer models. *J. Geophys. Res. Atmos.* **2008**, *113*, D13. [[CrossRef](#)]
32. Morcrette, J.-J.; Barker, H.W.; Cole, J.N.S.; Iacono, M.J.; Pincus, R. Impact of a New Radiation Package, McRad, in the ECMWF Integrated Forecasting System. *Mon. Weather Rev.* **2008**, *136*, 4773–4798. [[CrossRef](#)]
33. Price, E.; Mielikainen, J.; Huang, B.; Huang, H.A.; Lee, T. GPU acceleration experience with RRTMG longwave radiation model. In *High-Performance Computing in Remote Sensing III*; SPIE: Bellingham, WA, USA, 2013; pp. 71–82.
34. Zhang, H.; Nakajima, T.; Shi, G.; Suzuki, T.; Imasu, R. An optimal approach to overlapping bands with correlated k distribution method and its application to radiative calculations. *J. Geophys. Res. Atmos.* **2003**, *108*, D20. [[CrossRef](#)]
35. Zhang, H.; Suzuki, T.; Nakajima, T.; Shi, G.; Zhang, X.; Liu, Y. Effects of band division on radiative calculations. *Opt. Eng.* **2006**, *45*, 016002.
36. Zhou, Y.; Zhang, Y.; Li, J.; Yu, R.; Liu, Z. Configuration and evaluation of a global unstructured mesh atmospheric model (GRIST-A20.9) based on the variable-resolution approach. *Geosci. Model. Dev.* **2020**, *13*, 6325–6348. [[CrossRef](#)]
37. Wei, X.; Zhang, H. Analysis of Optical Properties of Nonspherical Dust Aerosols. *Acta Opt. Sin.* **2011**, *31*, 0501002.
38. Zhang, H.; Wang, Z.; Wang, Z.; Liu, Q.; Gong, S.; Zhang, X.; Shen, Z.; Lu, P.; Wei, X.; Che, H.; et al. Simulation of direct radiative forcing of aerosols and their effects on East Asian climate using an interactive AGCM-aerosol coupled system. *Clim. Dyn.* **2012**, *38*, 1675–1693. [[CrossRef](#)]
39. Nakajima, T.; Tsukamoto, M.; Tsushima, Y.; Numaguti, A.; Kimura, T. Modeling of the radiative process in an atmospheric general circulation model. *Appl. Opt.* **2000**, *39*, 4869–4878. [[CrossRef](#)] [[PubMed](#)]
40. Lu, P.; Zhang, H.; Li, J. Correlated k-Distribution Treatment of Cloud Optical Properties and Related Radiative Impact. *J. Atmos. Sci.* **2011**, *68*, 2671–2688. [[CrossRef](#)]

41. Fu, Q. An Accurate Parameterization of the Solar Radiative Properties of Cirrus Clouds for Climate Models. *J. Clim.* **1996**, *9*, 2058–2082. [[CrossRef](#)]
42. Yang, P.; Wei, H.; Huang, H.-L.; Baum, B.A.; Hu, Y.X.; Kattawar, G.W.; Mishchenko, M.I.; Fu, Q. Scattering and absorption property database for nonspherical ice particles in the near-through far-infrared spectral region. *Appl. Opt.* **2005**, *44*, 5512–5523. [[CrossRef](#)]
43. Baum, B.A.; Heymsfield, A.J.; Yang, P.; Bedka, S.T. Bulk Scattering Properties for the Remote Sensing of Ice Clouds. Part I: Microphysical Data and Models. *J. Appl. Meteorol.* **2005**, *44*, 1885–1895. [[CrossRef](#)]
44. Jing, X.; Zhang, H.; Peng, J.; Li, J.; Barker, H.W. Cloud overlapping parameter obtained from CloudSat/CALIPSO dataset and its application in AGCM with McICA scheme. *Atmos. Res.* **2016**, *170*, 52–65. [[CrossRef](#)]
45. Jing, X.; Zhang, H.; Satoh, M.; Zhao, S. Improving Representation of Tropical Cloud Overlap in GCMs Based on Cloud-Resolving Model Data. *J. Meteorol. Res.* **2018**, *32*, 233–245. [[CrossRef](#)]
46. Ebert, E.E.; Curry, J.A. A parameterization of ice cloud optical properties for climate models. *J. Geophys. Res. Atmos.* **1992**, *97*, 3831–3836. [[CrossRef](#)]
47. Slingo, A. A GCM Parameterization for the Shortwave Radiative Properties of Water Clouds. *J. Atmos. Sci.* **1989**, *46*, 1419–1427. [[CrossRef](#)]
48. Hong, G.; Yang, P.; Baum, B.A.; Heymsfield, A.J.; Xu, K.-M. Parameterization of Shortwave and Longwave Radiative Properties of Ice Clouds for Use in Climate Models. *J. Clim.* **2009**, *22*, 6287–6312. [[CrossRef](#)]
49. Yuan, J.; Fu, Q.; McFarlane, N. Tests and improvements of GCM cloud parameterizations using the CCCMA SCM with the SHEBA data set. *Atmos. Res.* **2006**, *82*, 222–238. [[CrossRef](#)]
50. Li, J.; Peng, X.; Li, X.; Lin, Y.; Chu, W. Evaluation of a Flexible Single Ice Microphysics and a Gaussian Probability-Density-Function Macrophysics Scheme in a Single Column Model. *Atmosphere* **2021**, *12*, 638. [[CrossRef](#)]
51. Zhang, Y.; Yu, R.; Li, J.; Li, X.; Rong, X.; Peng, X.; Zhou, Y. AMIP Simulations of a Global Model for Unified Weather-Climate Forecast: Understanding Precipitation Characteristics and Sensitivity Over East Asia. *J. Adv. Model. Earth Syst.* **2021**, *13*, e2021MS002592. [[CrossRef](#)]
52. Wild, M. The global energy balance as represented in CMIP6 climate models. *Clim. Dyn.* **2020**, *55*, 553–577. [[CrossRef](#)]

Disclaimer/Publisher’s Note: The statements, opinions and data contained in all publications are solely those of the individual author(s) and contributor(s) and not of MDPI and/or the editor(s). MDPI and/or the editor(s) disclaim responsibility for any injury to people or property resulting from any ideas, methods, instructions or products referred to in the content.